ChemCatChem

Research Article
doi.org/10.1002/cctc.202101702

Chemistry
Europe
European Chemical
Societies Publishing

www.chemcatchem.org

Utilization of Silver Silicate for the Formation of Highly Dispersed Silver on Silica Catalysts

Petra H. Keijzer,[a] Petra E. de Jongh,[a] and Krijn P. de Jong*[a]

Supported silver catalysts with small and uniform particle sizes are promising for selective hydrogenation or oxidation reactions. However, during catalyst preparation, transport of the silver precursors often leads to large silver particles, especially at higher silver loadings. In this paper, the use of silver silicate as an intermediate for the preparation of silica-supported silver nanoparticles is reported. Supported silver silicate was prepared by reacting silver nitrate with silica. Subsequently, the silver silicate was reduced to prepare supported silver nanoparticles of ~2 nm in size at a loading of 15 wt% Ag. The utilization of silver silicate limited the transport of silver species during precursor decomposition, resulting in silver nanoparticles 20 times smaller than those formed by direct reduction of a supported silver nitrate precursor. The catalysts were applied in carbon monoxide oxidation, which confirmed the high dispersion as well as the excellent stability of the supported silver nanoparticles thus prepared.

Introduction

Silver catalysts are used in industry on a large scale to produce formaldehyde from methanol, and to selectively oxidize ethylene to ethylene oxide.[1,2] For these reactions, either unsupported silver or silver supported on low surface area support material is used and the preferred size of silver structures exceeds 50 nm.[3–5] While supported silver nanoparticles below 10 nm do not (yet) have industrial applications as catalysts, they are interesting candidates for several selective oxidation and hydrogenation reactions, as the selectivity towards the desired products of the silver based catalysts is often superior to the more active catalysts based on platinum, palladium or gold.[6–9]

In industry, mostly impregnation and precipitation are used for the synthesis of heterogenous catalysts. Both techniques ensure a homogeneous distribution of the precursor over the support surface.[10] However, redistribution of the precursor both during the drying and precursor decomposition step may lead to large intra- and interparticle heterogeneities in the metal distribution, especially at relative high metal loadings.[11–14] Extensive research is dedicated to understanding and limiting this precursor redistribution. The use of model support materials with an ordered pore structure and narrow pore size distribution, such as SBA-15, is crucial for fundamental studies.[15–19]

There are several ways to prevent agglomeration of the metal during the decomposition step, including providing a stronger interaction between the support and the precursor or by changing decomposition parameters such as atmosphere and heating ramp to change the deactivation pathways.[20–23] Another way is to form an immobile intermediate, such as a metal silicate, to be further decomposed in a later step to form the desired metal nanoparticles.[24] By utilizing copper or nickel silicates as intermediates, supported copper or nickel catalysts with a high dispersion and narrow particle size were prepared, even at metal loadings up to 40 wt%.[12,25–29] To the best of our knowledge, deliberately utilizing the formation of silver silicate as intermediate in the preparation of supported silver catalysts has not yet been explored.

In literature, preparation routes for several different silver silicates can be found.[30–34] These silver silicate compounds are proposed as photocatalysts, where they show a higher activity compared to metallic silver.[35–42] Whereas the synthesis of pure and highly crystalline silver silicate generally takes place under high oxygen pressures, supported silver silicate can be synthesized by letting a silica source react with silver nitrate at atmospheric pressure.[43,44] Also during the synthesis of supported silver nanoparticles on silica, silver silicate may form. We observed the formation of silver silicate upon the synthesis of supported silver catalysts using melt infiltration of silica with molten silver nitrate.[19] Here, large crystallites of silver silicate were formed because of a high silver loading, which allowed us to identify the structure using X-ray diffraction. As the formation of silver silicate took place upon reacting silver nitrate and silica at elevated temperatures, many studies on the preparation of silica supported silver nanoparticles, probably unknowingly involved the formation and decomposition of silver silicate. In some studies, these silver silicate species were designated as silver oxide, even when the temperatures used during heat

[a] P. H. Keijzer, Prof. P. E. de Jongh, Prof. K. P. de Jong
Materials Chemistry and Catalysis
Debye Institute for Nanomaterials
Utrecht University
Universiteitsweg 99
3584 CG, Utrecht (The Netherlands)
E-mail: K.P.deJong@uu.nl

ChemCatChem

Research Article
doi.org/10.1002/cctc.202101702

Chemistry
Europe

European Chemical
Societies Publishing

treatments exceeded the decomposition temperature of silver oxides.[45–49]

In this paper, the use of silver silicate as an intermediate for the preparation of supported silver nanoparticles is discussed, also to better understand the role of silver silicate during the synthesis of supported silver catalyst. By using SBA-15 as model silica support material, we investigated both the formation of silver silicate in itself, and its influence on the structure of the SBA-15. Next, we studied the decomposition of silver silicate into highly dispersed silica-supported silver nanoparticles, and finally, the catalytic performance of these nanoparticles in the oxidation of carbon monoxide.

Results and Discussion

Silver silicate

The silver silicate formation was studied using X-ray diffraction (XRD). Figure 1, Frame A, shows the diffractograms of pristine SBA-15 (black line), and of SBA-15 impregnated with silver nitrate and heat treated at 400 °C in oxygen (dark orange line). The theoretical silver loading of this material was 55 wt% assuming full decomposition of the silver precursor. The diffractogram of pristine SBA-15 only shows a broad peak around 27°, known for amorphous silica. After impregnation and drying and a heat treatment at 400 °C in oxygen, sharp peaks especially in the region of 35–48° had formed, whereas the broad silica peak was no longer observed. In Figure C1 in the Supporting Information, the diffractogram is compared to the diffraction lines of silver oxide (AgO or Ag_2O) and other silver silicate materials, with Ag:Si ratios of 1–5. As in previous work,[19] the peak positions of the material obtained after the heat treatment shows an excellent match with the silver silicate crystal structure $Ag_{10}Si_4O_{13}$. The silver silicate had presumably formed following Reaction 1.
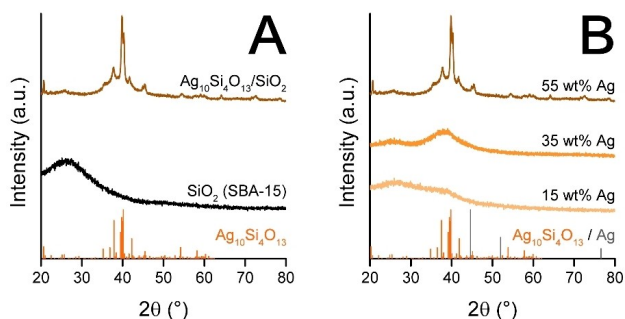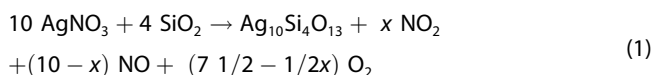
$$10\ AgNO_3 + 4\ SiO_2 \rightarrow Ag_{10}Si_4O_{13} + x\ NO_2$$
$$+ (10 - x)\ NO + (7\ 1/2 - 1/2x)\ O_2 \tag{1}$$

The sharp peaks of the silver silicate with the highest silver loading indicate the formation of large crystals. The temperature of the heat treatment (400 °C) was close to the decomposition temperature of the silver nitrate (440 °C). Both silver silicate and metallic silver formed when nitrogen was used during the thermal treatment (see Supporting Information, Figure C2). Therefore, to prevent the formation of metallic silver, it is important to perform the heat treatment in an oxygen-containing atmosphere. Presumably, the presence of oxygen stabilizes the molten silver nitrate.

In Frame B, diffractograms of materials containing silver silicate with varying theoretical silver loadings are shown. The broad silica-related peak at 27° is present in the materials containing 15 and 35 wt% silver, which shows that less silica had reacted than in the material containing 55 wt% silver, although the intensity of these peaks is still much lower compared to the peak at 27° in the diffractogram of pristine SBA-15. Furthermore, these diffractograms do not contain any sharp peaks. Instead, for both samples a broad peak around 42° is visible, which is ascribed to amorphous silver silicate.[50,51] A broad peak at this location has been ascribed to silver oxide in literature before.[45–49] As crystalline silver oxides decompose below or around 200 °C, it is highly unlikely to be present after the heat treatment at 400 °C. While the decomposition temperature of highly dispersed silver oxide with a high bonding strength to silica might be higher, the observed decrease in amorphous silica present cannot result from the formation of silver oxide alone. Moreover, the orange color of the material is in line with literature.[34,50,52] These considerations, and the location of the broad peak at 42° coinciding with the location of the most intense peaks of the silver silicate structure, confirm the formation silver silicate.

The pore structure of the silver silicate materials was investigated using N_2-physisorption. Figure 2 shows the isotherms (Frame A) and the pore volume distributions (Frame B) of pristine SBA-15 (black line) and the silver silicate materials (orange lines). Compared to pristine SBA-15 with a specific surface area of 890 $m_2 g_{SiO_2}^{-1}$ and pore volume of 1.15 $mL\,g_{SiO_2}^{-1}$, the surface area and volume of the silver silicate material containing 15 wt% silver had only slightly decreased to 590 $m^2 g_{SiO_2}^{-1}$ and 0.94 $mL\,g_{SiO_2}^{-1}$, respectively, indicating that
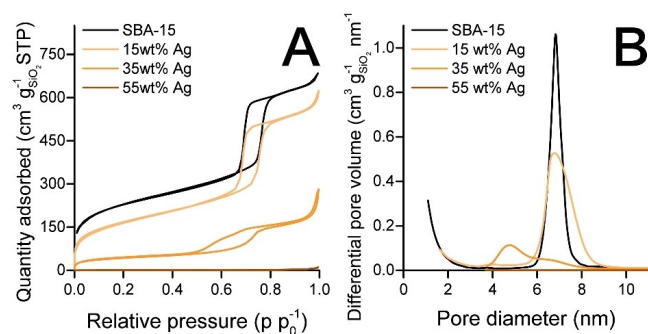

Figure 1. X-ray diffractograms of pristine SBA-15 (black line) and silver silicate structures with silver loadings of 55 wt% Ag (dark orange line), 35 wt% Ag (orange line) and 15 wt% Ag (light orange line). As reference, crystal structures of silver silicate (orange) and silver (grey) are added. The diffractograms are offset for clarity.


Figure 2. N_2-physisorption isotherms (Frame A) and pore size distributions (desorption, Frame B) of pristine SBA-15 and silver silicate materials varying in silver loading.

ChemCatChem

Research Article
doi.org/10.1002/cctc.202101702

Chemistry
**Europe**
European Chemical
Societies Publishing

no significant deformation of the structure had occurred. However, upon increasing the silver loading, the specific surface area and pore volume decreased drastically to respectively 170 $m^2 g_{SiO2}^{-1}$ and 0.42 mL g_{SiO2}^{-1} for 35 wt% silver, and 4 $m^2 g_{SiO2}^{-1}$ and 0.02 mL g_{SiO2}^{-1} for 55 wt% silver. Collapse of the porous structure was observed in bright field transmission electron microscopy (BF-TEM) images of these materials (see Supporting Information, Figure C3). While some porosity was still present in the material containing 35 wt% silver, complete destruction of the pore structure resulted in the loss of all porosity for the 55 wt% material.

Supported silver particles were formed upon thermal decomposition or reduction of the silver silicate. Figure 3 shows the results of thermal gravimetric analysis (TGA) combined with mass spectrometry (MS) measurements. In argon, the thermal decomposition of silver silicate started around 440 °C (Frame A), while the reduction in hydrogen already started around 125 °C (Frame B).

During the thermal decomposition of the silver silicate, oxygen was released, while during the reduction, water formed (MS signal, blue lines). No other decomposition products, such as NO_x, were detected (see Supporting Information, Figure D1). The absence of these NO_x products during the decomposition of silver silicate was in contrast with the NO and NO_2 that evolved upon heating supported silver nitrate (see Supporting Information, Figure D2), indicating that all silver nitrate had been converted during the heat treatment at 400 °C. The TGA-MS data show multiple decomposition steps, both during the thermal decomposition and the reduction. Probably some intermediate silver silicate structures varying in Ag:Si:O ratio formed during the decomposition process as has been reported before.[30] The overall thermal decomposition and reduction of the silver silicate presumably takes place via Reactions 2 and 3, respectively. Considering these reactions and the silver weight loading, a weight loss of circa 4% was expected, which is in line with the measured weight loss of about 5% in both cases.

$$Ag_{10}Si_4O_{13} \rightarrow 10\ Ag^0 + 4\ SiO_2 + 2\ 1/2\ O_2 \qquad (2)$$
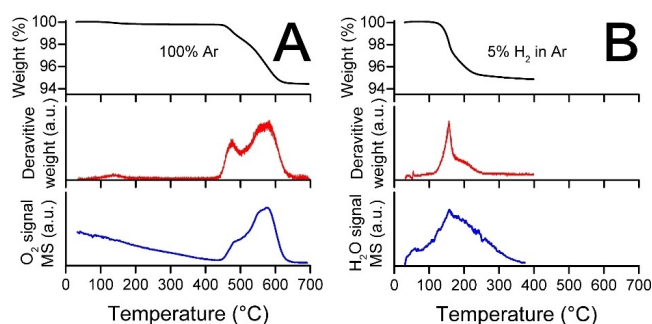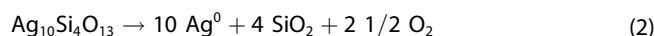
Figure 3. Decomposition of silver silicate with 55 wt% silver followed using TGA-MS with a heating ramp of 5 °C min⁻¹. The weight (black line) and the derivative of the weight (red line) indicate the decomposition of silver silicate starting around 440 °C in inert atmosphere (A), and around 125 °C in reductive atmosphere (B). The MS signals (blue line) show the formation of oxygen or water during the decomposition in nitrogen or hydrogen, respectively.

$$Ag_{10}Si_4O_{13} + 5\ H_2 \rightarrow 10\ Ag^0 + 4\ SiO_2 + 5\ H_2O \qquad (3)$$
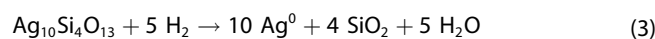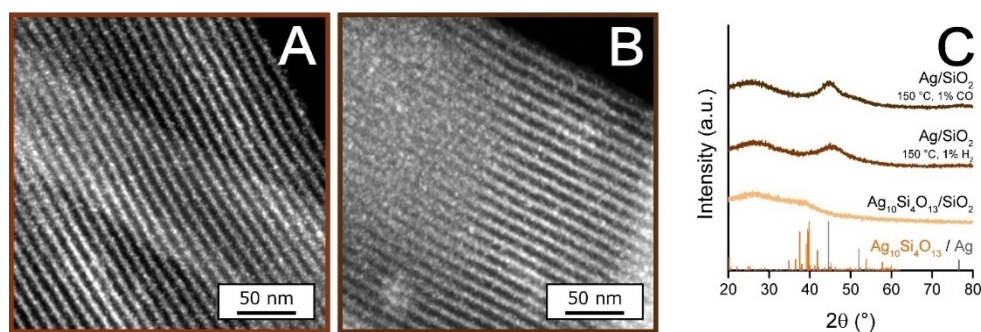
Preparation of supported silver catalysts

Decomposition of silver silicate via reduction for the materials containing 35 wt% or 55 wt% silver resulted in the formation of metallic silver with a broad particle size distribution (see Supporting Information, Figure E1). We were not able to prepare catalysts with a uniform silver particle size as result of the tremendous decrease in surface area of the silica support material in combination with the high silver loading. Therefore, for the preparation of supported silver catalysts, we focused on materials containing 15 wt% silver. Supported silver nanoparticles were prepared via silver silicate, and, as reference, via the direct reduction of silver nitrate on SBA-15. Both hydrogen and carbon monoxide were used to reduce the silver silicate. Table 1 summarizes the particle and crystallite sizes of all obtained supported silver nanoparticles discussed below.

Figure 4 shows high-angle annular dark-field scanning transmission electron microscopy (HAADF-STEM) images of the materials after reduction of silver silicate at 150 °C in 1% hydrogen (15 Ag_SN_SS-1H₂, Frame A) or 1% carbon monoxide (15 Ag_SN_SS-1CO, Frame B) and their XRD diffractograms (Frame C). At the peak position of metallic silver, broad peaks are visible in the diffractograms of both reduced materials, while the broad peak around 42° is no longer visible. This shows that in both cases the reductions of the silver silicate resulted in the formation of metallic silver nanoparticles. In the HAADF-STEM figures, next to the pore structure of the SBA-15, ultra-fine, highly dispersed white dots are visible, which are the metallic silver nanoparticles. The surface averaged diameters of the nanoparticle, 1.6 nm ± 0.4 nm for H_2 reduced and 1.8 nm ± 0.5 nm for CO reduced, match the calculated crystallite sizes of the silver (see Table 1).

The high dispersion of the silver over the support made it possible to reform silver silicate, upon additional treatment at 400 °C in oxygen atmosphere for 2 h. Figure 5 shows the diffractograms of silver silicate material, and of 15 Ag_SN_SS-1CO before and after receiving consecutive heat treatments in oxidizing (15 Ag_SN_SS-1CO_O) and reducing atmosphere (15 Ag_SN_SS-1CO_OR) in Frame A, and a HAADF-STEM image of the material obtained after the last heat treatment in

Table 1. Overview of crystallite sizes and surface averaged diameters of silver nanoparticles supported on SBA-15, labeled in the form of *wt*%Ag_ *P_D_*OR, with wt% being the theoretical silver weight loading, *P* the precursor(s) (SN = silver nitrate, SS = silver silicate), *D* the atmosphere during decomposition, and OR standing for extra oxidation and reduction treatments, if applicable. The crystallite sizes were obtained via XRD and particle diameters via HAADF-STEM analysis. See Supporting Information, Section A, for particle size distributions and fits of XRD diffractograms.

Material	Crystallite size [nm]	Diameter [nm]
15 Ag_SN_SS-1H₂	1.3	1.6 ± 0.4
15 Ag_SN_SS-1CO	1.6	1.8 ± 0.5
15 Ag_SN_SS-1CO_OR	1.7	1.5 ± 0.3
15 Ag_SN-1H₂	32	33 ± 13

ChemCatChem

Research Article
doi.org/10.1002/cctc.202101702

Chemistry
Europe
European Chemical
Societies Publishing

Figure 4. HAADF-STEM images of the supported silver nanoparticles containing 15 wt% silver obtained via reduction of silver silicate in 1% hydrogen (15 Ag_SN_SS-1H_2, A) or 1% carbon monoxide (15 Ag_SN_SS-1CO, B) and XRD diffractograms of the silver silicate before and after corresponding reductions (C). As reference, crystal structures of silver silicate (orange) and silver (grey) are added. The diffractograms are offset for clarity.
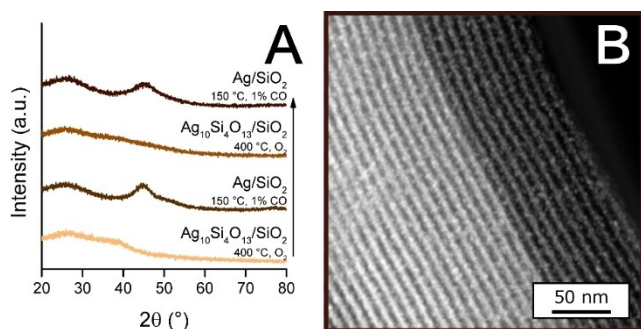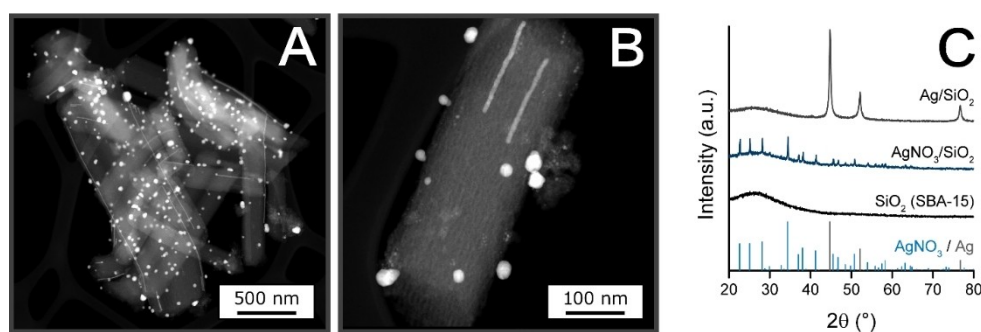

Figure 5. XRD diffractograms of silver containing structures after various consecutive heat treatments in oxidizing or reducing atmosphere (A) and a HAADF-STEM image of the last material formed (15 Ag_SN_SS-1CO_OR, B). The diffractograms are offset for clarity.

Frame B. Upon treating 15 Ag_SN_SS-1CO at 400 °C in oxygen atmosphere, the broad peak around 42°, indicative of silver silicate, had reformed and peaks corresponding to metallic silver could no longer be detected. The redispersion of silver over support materials, including the formation of silver silicate from silver oxide and silica, has been reported in literature before.[30,32,53–55] However, these changes generally occurred only at high temperatures and/or high oxygen pressures. In our case, due to the high dispersion of the metallic silver over the

support, the silver silicate structure could be reformed under relative mild oxidative conditions (atmospheric pressure, 400 °C in oxygen).

A second reductive treatment on the reformed silver silicate at 150 °C in 1% carbon monoxide again led to the formation of metallic silver (15 Ag_SN_SS-1CO_OR). As shown in Figure 5, Frame B, the metallic silver once more was homogeneously distributed over the silica support, in the form of silver nanoparticles. With their surface averaged diameter of 1.5 nm ± 0.3 nm, these particles were similar in size to the prepared silver nanoparticles before the two additional heat treatments.

The size and dispersion of the supported silver nanoparticles prepared via silver silicate as intermediate are remarkable, especially considering the relatively high silver loading of 15 wt%. To substantiate the effect of utilizing the formation of silver silicate, a reference catalyst, also containing 15 wt% silver, was prepared without the formation of silver silicate. SBA-15 containing silver nitrate was directly reduced at 150 °C, in a flow of 1% hydrogen in nitrogen flow (15 Ag_SN-1H_2). Figure 6 shows HAADF-STEM images of this material and XRD diffractograms of the material before and after reduction. The XRD diffractogram of the reduced material shows sharp peaks with a high intensity at the peak location of silver, indicative of relatively large silver crystals. Silver particles are clearly visible in the HAADF-STEM images, with a surface averaged diameter of

Figure 6. HAADF-STEM images of silica-supported silver nanoparticles containing 15 wt% silver obtained via reduction of silver nitrate in 1% H_2 (15 Ag_SN-1H_2, A, B) and XRD diffractograms of SBA-15, SBA-15 impregnated with silver nitrate and this material upon reduction in 1% H_2 (C). As reference, crystal structures of silver nitrate (blue) and silver (grey) are added. The diffractograms are offset for clarity.

ChemCatChem

Research Article
doi.org/10.1002/cctc.202101702

Chemistry Europe
European Chemical
Societies Publishing

33 ± 13 nm. In contrast to the materials prepared via silver silicate, no silver particles below 2 nm were for 15 Ag_SN-1H$_2$. Next to silver particles, also some silver nanowires had formed. While the wires were located inside the pores of the SBA-15, most of the silver particles were located on the outside of the SBA-15 particles, as is visible in Frame B. This means that transport of the silver precursor had occurred. The formation of these large particles is similar to the formation of silver particles on the external surface of the SBA-15 particles, as reported by Mikheeva *et al.* for their reference Ag/SBA-15 catalyst.[56] Direct reduction of the silver nitrate led to redistribution of the silver precursor, with an inhomogeneous distribution of the silver over the support as result. Moreover, this led to a 20-fold increase in silver particle size compared to the materials prepared via the silver silicate route.
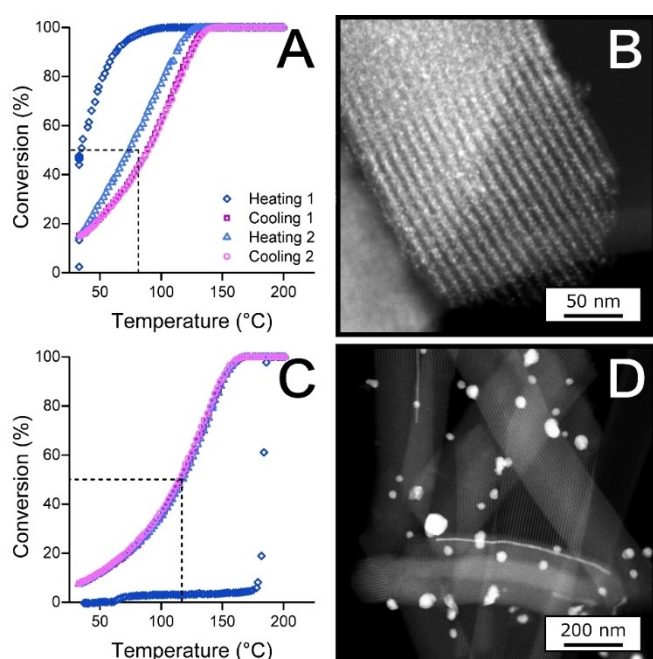
Figure 7. Conversion of carbon monoxide versus the reaction temperature increase/decrease (1 °C min^{-1}) in carbon monoxide oxidation (25 mg catalyst, gas flow rate of 320 L g$_{Ag}$$^{-1}$ h^{-1}) using 15 Ag_SN_SS-1CO (A) or 15 Ag_SN-1H$_2$ (C) and HAADF-STEM images of the used catalysts, respectively (B, D).

CO oxidation

The catalysts were investigated for the oxidation of carbon monoxide to carbon dioxide. The catalytic runs consist of four heating and cooling cycles, two with a gas flow rate of 320 L g$_{Ag}$$^{-1}$ h^{-1}, and then two with a gas flow rate of 640 L g$_{Ag}$$^{-1}$ h^{-1}. Figure 7 shows the performance of the catalysts during the first two heating and cooling cycles and HAADF-STEM images of the used catalysts, the catalytic performance during the last two cycles is given in Supporting Information, Figure F1. The catalytic performance of silver silicate reduced using 1% CO in helium (similar to 15 Ag_SN_SS-1CO) is shown in Frame A. The reduction of the silver silicate was performed in the CO oxidation setup, to prevent oxidation of the silver particles before the catalysis started. Directly after the reduction, the catalyst showed a high activity already at room temperature, with 50% conversion of carbon monoxide at 35 °C and complete conversion around 100 °C. This high activity was only observed during the first heating. After the first heating, the activity of the catalyst was lower, and hysteresis was observed.

The catalytic performance of 15 Ag_SN-1H$_2$ is given in Figure 7, Frame C. The activity during the first heating was much lower compared to the activities observed during later heating and cooling. In this case, the catalyst had been exposed to air prior to the catalytic reaction, as the reduction was performed ex-situ. A small silver oxide layer presumably covered the silver nanoparticles, which limited the catalytic activity. Once a temperature of circa 180 °C was reached, the silver oxide decomposed to form the metallic silver and the conversion changed in two minutes time from almost none to full conversion.

In Table 2, the temperatures at which 50% of the carbon monoxide was converted ($T_{X=50\%}$) are listed, and Table 3 summarizes the turnover frequency (TOF), calculated reaction orders and activation energy of both catalysts (for more details, see Supporting Information, Section B). The TOFs per total amount of silver were comparable with values reported in literature.[48,57] The reaction order of carbon monoxide was higher than oxygen, indicating a lower CO coverage at the silver surface. For 15 Ag_SN_SS-1CO, the difference in $T_{X=50\%}$ between the heating and cooling was 15 °C for both gas flow

Table 2. $T_{X=50\%}$ in the different heating and cooling ramps during carbon monoxide oxidation reactions.

| Catalyst | $T_{X=50\%}$, gas flow rate = 320 L g$_{Ag}$$^{-1}$ h^{-1} | | | | $T_{X=50\%}$, gas flow rate = 640 L g$_{Ag}$$^{-1}$ h^{-1} | | | |
	Heating 1	Cooling 1	Heating 2	Cooling 2	Heating 3	Cooling 3	Heating 4	Cooling 4
15 Ag_SN_SS-1CO	35 °C	90 °C	75 °C	90 °C	85 °C	100 °C	85 °C	100 °C
15 Ag_SN-1H$_2$	183 °C	118 °C	115 °C	118 °C	130 °C	130 °C	130 °C	130 °C

Table 3. Reaction orders, activation energies and turnover frequencies during carbon monoxide oxidation reactions obtained using a gas flow rate of 640 L g$_{Ag}$$^{-1}$ h^{-1}.

Catalyst	Reaction order CO	Reaction order O$_2$	Activation energy [kJ mol^{-1}]	TOF$_{T=50°C}$ [mol$_{CO}$ mol$_{Ag,total}$$^{-1}$ h^{-1}]	TOF$_{T=50°C}$ [mol$_{CO}$ mol$_{Ag,surface}$$^{-1}$ h^{-1}]
15 Ag_SN_SS-1CO	0.56	0.27	23.3	3.1	4.6
15 Ag_SN-1H$_2$	0.61	0.10	27.6	1.8	50

ChemCatChem

Research Article
doi.org/10.1002/cctc.202101702

**Chemistry
Europe**
European Chemical
Societies Publishing

rates, while the activity did not change significantly during heating or cooling for 15 Ag_SN-1H$_2$. Additionally, the reaction order in carbon monoxide was similar for both catalysts, while the reaction order in oxygen was higher for 15 Ag_SN_SS-1CO. This shows that these smaller silver particles were more sensitive to changes in oxygen concentration than the much larger silver particles present in 15 Ag_SN-1H$_2$.

The activity, considered per mol of silver surface, was about 10 times lower on the small silver particles present in 15 Ag_SN_SS-1CO, than on the larger silver particles present in 15 Ag_SN-1H$_2$. Presumably, these larger particles were more metallic in nature, which caused a higher activity per active site. However, with a difference in T$_{X=50\%}$ of 30–45 °C, a higher overall activity was obtained for 15 Ag_SN_SS-1CO than 15 Ag_SN-1H$_2$, (see Table 2). This higher activity mainly results from the large number of active sites, facilitated by the high silver dispersion.

The higher activity on metallic silver surfaces may also explain the higher activity observed during the first heating, and the difference in activity observed during heating and cooling for 15 Ag_SN_SS-1CO (Figure 7, Frame A). Directly after reduction of the silver silicate, the small silver nanoparticles were fully metallic, and showed a high catalytic activity. However, during catalysis, presumably the silver surface oxidation state and/or surface coverage of these highly dispersed silver nanoparticles changed, which in turn changed their activity. Presumably, upon continuous heating or cooling, the time needed for equilibrizing was larger than the heating or cooling ramp provided. When the reaction temperature was heated stepwise, and kept at each temperature for a while, no differences in activity upon heating or cooling were observed (see Supporting Information, Figure F2). The corresponding measured conversion levels lied in between the those measured during continuous heating or cooling.

Despite the change in surface coverage, the activity did not change over time apart from the first heating only for 15 Ag_SN-1H$_2$ and for the additional differences in activity between heating and cooling for 15 Ag_SN_SS-1CO (see Supporting Information, Figure F1). Both catalysts therefore showed an excellent stability. The high stability of the silver nanoparticles was validated using HAADF-STEM analysis, in Figure 7, Frame B and C, images of the used catalysts are shown. The surfaced average silver particle sizes of the used catalysts were 1.7 nm ± 0.4 nm and 33 nm ± 11 nm for 15 Ag_SN_SS-1CO and 15 Ag_SN-1H$_2$, respectively. After heating several times to 200 °C, their sizes were the same as the freshly prepared catalysts shown in Figure 4.

Conclusion

During the preparation of silica-supported silver catalysts, redistribution of the silver precursor can lead to an inhomogeneous distribution of the silver and the formation of large silver particles. We show the merit of utilizing the formation of silver silicate as an intermediate instead of directly decomposing the silver precursor into its metallic state. Transport of the silver was restricted by first letting the silver precursor, silver nitrate,

react with the silica to form silver silicate. This enabled the preparation of highly dispersed silver nanoparticles on silica, even at 15 wt% silver. Silver silicate is readily formed upon heating impregnated silica with silver nitrate in an oxygen-containing atmosphere. For extreme silver loadings of 55 wt%, the formation of crystalline silver silicate in the form of Ag$_{10}$Si$_4$O$_{13}$ was observed, which deformed the pore structure of the silica. However, no deformation of the SBA-15 structure was observed when the silver loading was 15 wt%. Highly dispersed supported silver nanoparticles with a particle size of 1.6 nm and a narrow particle size distribution were obtained. The average size of the obtained silver was 20 times smaller than supported silver particles prepared via direct reduction of silver nitrate on SBA-15. Due to the large number of active sites, the catalyst prepared via silver silicate showed a higher overall catalytic activity in the oxidation of carbon monoxide compared to the catalyst prepared via direct reduction of the silver nitrate. Moreover, the catalyst showed excellent stability, and no particle growth was observed. In conclusion, utilization of silver silicate allows the preparation of ultra-fine, highly dispersed supported silver nanoparticles, even at high silver loadings. The excellent stability of these silver nanoparticles during the oxidation of carbon monoxide makes them promising candidates for oxidation and possibly also for hydrogenation reactions.

Experimental Section

Synthesis of the support

SBA-15 was prepared via a sol-gel synthesis, according to the procedure described before.[19] 23.4 g Pluronic P123 (EO$_{20}$PO$_{70}$EO$_{20}$, average Mw = 5800, Aldrich) was dissolved in 606.8 g deionized water and 146.4 g hydrochloric acid (HCl, 37 wt%, fuming, Merck, analysis grade) in a 1 L polypropylene bottle (cylindrical, height 19.7 cm, diameter 10.5 cm). After the mixture was vigorously stirred for at least 3 hours in an oil bath at 55 °C, the stirring rate was set to 600 rpm (PFTE stirring bar, 50×7 mm) and 50 g tetraethyl orthosilicate (TEOS, >99%, Aldrich) was added at once. After 2 min, the stirring bar was removed and the lid of the bottle was closed tightly. The mixture was first kept for 24 h at 55 °C, then for 24 h at 90 °C. Next, the material was filtrated and washed with deionized water using a Büchner funnel until the pH of the filtrate was around 5–6 (and hence no HCl was left in the solution). The filtrate was dried at 60 °C for 2–3 days and afterwards crushed into a fine powder and calcined at 550 °C for 6 h (heating ramp 1 °C min^{-1}) in static air.

Synthesis of silver silicate

A silver precursor was deposited on the SBA-15 via incipient wetness impregnation. In a typical synthesis, the SBA-15 powder was dried under dynamic vacuum in a round bottom flask at 200 °C for 2 hours. Silver nitrate (99 + %, Sigma-Aldrich) was dissolved in demineralized water. The amount of demineralized water was 90% of the pore volume of the support. The amount of silver nitrate was adjusted to obtain materials with a calculated loading of 15, 35 or 55 wt% silver upon full decomposition of the silver precursor. The precursor solution was added dropwise to the support material, under vacuum. A uniform distribution of the precursor solution

ChemCatChem

Research Article
doi.org/10.1002/cctc.202101702

Chemistry
Europe
European Chemical
Societies Publishing

over the support was facilitated by stirring the powder using a stirring bar. After addition of the precursor, the material was dried overnight under dynamic vacuum at room temperature, under continuous stirring. The dried material, white powder (75–150 μm), was heated to 400 °C (2–6 hours, 2 °C min^{-1} heating ramp) in 100 % oxygen or nitrogen flow. The temperature chosen is in between the melting temperature (212 °C) and the decomposition temperature (440 °C) of silver nitrate. After this heat treatment, the color of the material was orange, with a darker orange to brown-red color for materials with a higher silver loading.

Synthesis of supported silver nanoparticles

The silver silicate powder was treated at 150 °C (1 hour, 0.5 °C min^{-1} heating ramp) in a flow of 1–10 % carbon monoxide or hydrogen in nitrogen to decompose the silver precursor. A reference catalyst with a calculated loading of 15 wt% Ag was prepared by direct reduction of silver nitrate on SBA-15 after impregnation and drying. For this, SBA-15 was impregnated with silver nitrate and dried overnight, the same way as described above, then treated at 150 °C (1 hour, 0.5 °C min^{-1} heating ramp) in a flow of 1 % hydrogen in nitrogen.

Characterization

The pore size, pore volume and surface area of the materials were analyzed using N$_2$-physisorption. Isotherms were measured at -196 °C on a Micromeritics TriStar 3000 apparatus. The specific surface area of the support was calculated using the BET equation (0.05 < p/p$_0$ < 0.25). The support material and silver containing materials were analyzed by bright field transmission electron microscopy (BF-TEM) and by high-angle annular dark-field scanning transmission electron microscopy (HAADF-STEM) using the Talos L120 C and Talos F200X microscopes, operated at 120 and 200 kV, respectively. The samples were prepared by dispersing a dry powder onto a TEM grid, or via dropwise addition of a dispersion of the material in ethanol obtained by sonication to a TEM grid. To limit decomposition of silver silicate materials by the electron beam, the TEM grids containing these materials and grid holder were cooled with liquid nitrogen to circa -180 °C during the measurements. Crystal phase analysis was performed using X-Ray Diffraction (XRD) on a Bruker D2 Phaser diffractometer, equipped with a Co K$_\alpha$ source (λ = 0.1789 nm). The composite structures were analyzed by comparing the XRD diffractograms with crystal structures from the PDF-4 + 2016 database. Crystallite sizes were calculated from fits made using TOPAS V5 software. For details on the surface averaged particle sizes and the particle size distributions obtained using TEM, and on the calculated crystallite sizes using XRD and TOPAS, see Supporting Information, Section A. The weight loss of silver silicate during heating was determined using thermal gravimetric analysis (TGA) performed in a Perkin Elmer TGA 8000 equipped with a mass spectrometer (MS). 10-30 mg material was heated up to 700 °C (5 °C min^{-1} heating ramp) in a flow of argon or 5 % hydrogen in argon (100 mL min^{-1}).

Catalytic testing

The catalytic performance of supported silver catalysts was investigated for the oxidation of carbon monoxide. In a typical catalysis experiment, 25 mg of catalyst grains (75–150 μm) diluted with 200 mg SiC (212–425 μm) was loaded in a plug flow reactor with an inner diameter of 4 mm between two layers of quartz wool. The reaction was carried out at 30–200 °C (1 °C min^{-1} heating ramp) at atmospheric pressure, in a flow of 20 or 40 mL min^{-1} containing 1 % carbon monoxide and 1 % oxygen in helium, resulting in a gas

flow rate of 320 or 640 L g$_{Ag}^{-1}$ h^{-1}. For the determination of the reaction order, the reaction was carried out at 50 °C, with a gas flow rate of 640 L g$_{Ag}^{-1}$ h^{-1} and the concentration of carbon monoxide or oxygen was varied between 0.5 % and 1.5 %, while keeping the concentration of the other reactant at 1 %. The reaction products were analyzed every 2 min using online gas chromatography (Interscience) equipped with two separate channels containing an MXT-Msieve 5 A column and an MXT-Q column, two thermal conductivity detectors and a flame ionization detector. For details on how the conversion, reaction orders and activation energies were calculated, see Supporting Information, Section B.

Conflict of Interest

The authors declare no conflict of interest.

Data Availability Statement

The data that support the findings of this study are available from the corresponding author upon reasonable request.

[1] I. E. Wachs, R. J. Madix, *Surf. Sci.* **1978**, *76*, 531–558.
[2] M. O. Özbek, I. Onal, R. A. Van Santen, *J. Catal.* **2011**, *284*, 230–235.
[3] G. J. Millar, M. Collins, *Ind. Eng. Chem. Res.* **2017**, *56*, 9247–9265.
[4] J. E. van den Reijen, S. Kanungo, T. A. J. Welling, M. Versluijs-Helder, T. A. Nijhuis, K. P. de Jong, P. E. de Jongh, *J. Catal.* **2017**, *356*, 65–74.
[5] L. G. Pinaeva, A. S. Noskov, *Pet. Chem.* **2020**, *60*, 1191–1206.
[6] P. Claus, H. Hofmeister, *J. Phys. Chem. B* **1999**, *103*, 2766–2775.
[7] X. Yang, A. Wang, X. Wang, T. Zhang, K. Han, J. Li, *J. Phys. Chem. C* **2009**, *113*, 20918–20926.
[8] V. V. Torbina, A. A. Vodyankin, S. Ten, G. V. Mamontov, M. A. Salaev, V. I. Sobolev, O. V. Vodyankina, *Catalysts* **2018**, *8*, DOI 10.3390/catal8100447.
[9] C. Wen, A. Yin, W. L. Dai, *Appl. Catal. B* **2014**, *160–161*, 730–741.
[10] P. Munnik, P. E. de Jongh, K. P. de Jong, *Chem. Rev.* **2015**, *115*, 6687–6718.
[11] E. Plessers, J. E. van den Reijen, P. E. de Jongh, K. P. de Jong, M. B. J. Roeffaers, *ChemCatChem* **2017**, *9*, 4562–4569.
[12] C. E. Pompe, M. Slagter, P. E. de Jongh, K. P. de Jong, *J. Catal.* **2018**, *365*, 1–9.
[13] T. M. Eggenhuisen, H. Friedrich, F. Nudelman, J. Zec, N. A. J. M. Sommerdijk, P. E. de Jongh, K. P. de Jong, *Chem. Mater.* **2013**, *25*, 890–896.
[14] T. Toupance, M. Kermarec, C. Louis, *J. Phys. Chem. B* **2000**, *104*, 965–972.
[15] J. R. A. Sietsma, J. D. Meeldijk, M. Versluijs-Helder, A. Broersma, A. Jos Van Dillen, P. E. de Jongh, K. P. de Jong, *Chem. Mater.* **2008**, *20*, 2921–2931.

[16] R. M. Rioux, H. Song, J. D. Hoefelmeyer, P. Yang, G. A. Somorjai, *J. Phys. Chem. B* **2005**, *109*, 2192–2202.

[17] A. Martínez, C. López, F. Márquez, I. Díaz, *J. Catal.* **2003**, *220*, 486–499.

[18] S. Singh, R. Kumar, H. D. Setiabudi, S. Nanda, D. V. N. Vo, *Appl. Catal. A* **2018**, *559*, 57–74.

[19] P. H. Keijzer, B. Donoeva, K. P. de Jong, P. E. de Jongh, *Catal. Today* **2021**, *375*, 393–400.

[20] H. Hu, S. Lu, T. Li, Y. Zhang, C. Guo, H. Zhu, Y. Jin, M. Du, W. Zhang, *Nanoscale Adv.* **2021**, *3*, 1865–1886.

[21] S. Eskandari, A. Dong, L. T. De Castro, F. Bin, A. B. Rahman, J. Lipp, D. A. Blom, J. R. Regalbuto, *Catal. Today* **2019**, *338*, 60–71.

[22] M. Wolters, L. J. W. Van Grotel, T. M. Eggenhuisen, J. R. A. Sietsma, K. P. de Jong, P. E. de Jongh, *Catal. Today* **2011**, *163*, 27–32.

[23] P. Munnik, M. Wolters, A. Gabrielsson, S. D. Pollington, G. Headdock, J. H. Bitter, P. E. De Jongh, K. P. De Jong, *J. Phys. Chem. C* **2011**, *115*, 14698–14706.

[24] Z. Bian, S. Kawi, *Catal. Today* **2020**, *339*, 3–23.

[25] L. F. Chen, P. J. Guo, M. H. Qiao, S. R. Yan, H. X. Li, W. Shen, H. L. Xu, K. N. Fan, *J. Catal.* **2008**, *257*, 172–180.

[26] J. Gong, H. Yue, Y. Zhao, S. Zhao, L. Zhao, J. Lv, S. Wang, X. Ma, *J. Am. Chem. Soc.* **2012**, *134*, 13922–13925.

[27] F. Dong, G. Ding, H. Zheng, X. Xiang, L. Chen, Y. Zhu, Y. Li, *Catal. Sci. Technol.* **2016**, *6*, 767–779.

[28] H. Liu, H. Wang, J. Shen, Y. Sun, Z. Liu, *Appl. Catal. A* **2008**, *337*, 138–147.

[29] P. Burattin, M. Che, C. Louis, *J. Phys. Chem. B* **2000**, *104*, 10482–40489.

[30] W. Klein, M. Jansen, *Zeitschrift fur Anorg. und Allg. Chemie* **2008**, *634*, 1077–1081.

[31] E. Thilo, F. Wodtcke, *ZAAC* **1958**, *295*, 247–261.

[32] M. Jansen, H.-L. Keller, *Angew. Chem.* **1979**, *91*, 500–500; *Angew. Chem. Int. Ed.* **1979**, *18*, 470–471.

[33] K. Heidebrecht, M. Jansen, *ZAAC* **1991**, *597*, 79–86.

[34] A. Al-Keisy, L. Ren, D. Cui, Z. Xu, X. Xu, X. Su, W. Hao, S. X. Dou, Y. Du, *J. Mater. Chem. A* **2016**, *4*, 10992–10999.

[35] L. Wang, J. Wu, *Inorg. Chem. Commun.* **2021**, *129*, 108619.

[36] R. Cao, H. Yang, X. Deng, S. Zhang, X. Xu, *Sci. Rep.* **2017**, *7*, 1–12.

[37] Y. Wang, Y. Jing, W. Li, M. Yu, X. Ao, Y. Xie, Q. Chen, *RSC Adv.* **2018**, *8*, 23442–23450.

[38] T. G. Kim, D. H. Yeon, T. Kim, J. Lee, S. J. Im, *Appl. Phys. Lett.* **2013**, *103*, 1–5.

[39] M. V. Baidakova, N. A. Germanov, S. N. Golyandin, M. E. Kompan, S. V. Mochalov, A. V. Nashchekin, V. N. Nevedomskii, S. A. Pul'nev, M. K. Rabchinskii, V. P. Ulin, N. V. Ulin, *Tech. Phys.* **2019**, *64*, 884–892.

[40] Z. Lou, B. Huang, Z. Wang, X. Ma, R. Zhang, X. Zhang, X. Qin, Y. Dai, M. H. Whangbo, *Chem. Mater.* **2014**, *26*, 3873–3875.

[41] M. T. Galante, P. Sotelo, M. K. Hossain, A. Vali, A. Raamann, C. Longo, R. T. Macaluso, K. Rajeshwar, *ChemElectroChem* **2019**, *6*, 87–96.

[42] X. Zhu, P. Wang, B. Huang, X. Ma, X. Qin, X. Zhang, Y. Dai, *Appl. Catal. B* **2016**, *199*, 315–322.

[43] X. Cui, S. H. Yu, L. Li, K. Li, B. Yu, *Adv. Mater.* **2004**, *16*, 1109–1112.

[44] J. Liu, W. Wu, Q. Tian, Z. Dai, Z. Wu, X. Xiao, C. Jiang, *Dalton Trans.* **2016**, *45*, 12745–12755.

[45] X. Zhang, Z. Qu, X. Li, M. Wen, X. Quan, D. Ma, J. Wu, *Sep. Purif. Technol.* **2010**, *72*, 395–400.

[46] Z. Qu, M. Cheng, W. Huang, X. Bao, *J. Catal.* **2005**, *229*, 446–458.

[47] K. A. Bethke, H. H. Kung, *J. Catal.* **1997**, *172*, 93–102.

[48] V. V. Dutov, G. V. Mamontov, V. I. Zaikovskii, L. F. Liotta, O. V. Vodyanki-na, *Appl. Catal. B* **2018**, *221*, 598–609.

[49] G. Corro, U. Pal, E. Ayala, E. Vidal, *Catal. Today* **2013**, *212*, 63–69.

[50] Z. Lou, Z. Wang, B. Huang, Y. Dai, G. Wang, Z. Jiang, X. Zhang, X. Qin, Y. Li, *Chem. A Eur. J.* **2015**, *21*, 8706–8710.

[51] S. Zhang, H. Gao, X. Liu, Y. Huang, X. Xu, N. S. Alharbi, T. Hayat, J. Li, *ACS Appl. Mater. Interfaces* **2016**, *8*, 35138–35149.

[52] M. Jansen, *Angew. Chem. Int. Ed. Engl.* **1987**, *26*, 1098–1110.

[53] H. Beyer, P. A. Jacobs, J. B. Uytterhoeven, *J. Chem. Soc. Faraday Trans. 1* **1976**, *72*, 674–685.

[54] L. R. Gellens, W. J. Mortier, J. B. Uytterhoeven, *Zeolites* **1981**, *1*, 85–90.

[55] K. ichi Shimizu, K. Sawabe, A. Satsuma, *ChemCatChem* **2011**, *3*, 1290–1293.

[56] N. N. Mikheeva, V. I. Zaikovskii, Y. V. Larichev, G. V. Mamontov, *Mater. Today Chem.* **2021**, *21*, 100530.

[57] X. Zhang, H. Dong, Y. Wang, N. Liu, Y. Zuo, L. Cui, *Chem. Eng. J.* **2016**, *283*, 1097–1107.